Unraveling Oxygen Vacancy-Driven Catalytic Hydrogen Evolution Activity and Stability over Atomic-Layer-Deposited Platinum Cluster Catalysts

Xinshuo Zhao,[a,#] Xiangbin Kong,[b,#] Ruokun Zhang,[a] Hao Xu,[a] Jiawei Yao,[a] Yutong Feng,[a] Yurong He,[b,*] Yong Qin,[c,*] Jiankang Zhang[a,*]

[a] Interdisciplinary Research Center of Biology & Catalysis, School of Life Science and Technology, Northwestern Polytechnical University, Xi'an 710072, P. R. China

[b] State Key Laboratory of High-efficiency Coal Utilization and Green Chemical Engineering, College of Chemistry and Chemical Engineering, Ningxia University, Yinchuan 750000, P. R. China.

[c] State Key Laboratory of Advanced Optical Polymer and Manufacturing Technology, College of Materials Science and Engineering, Qingdao University of Science and Technology, Qingdao 266042, P. R. China

[#] These authors contributed equally to this work.

[*] Corresponding authors. E-mail addresses: hyr@nxu.edu.cn; qinyong@qust.edu.cn; zhangjiankang@nwpu.edu.cn

Experimental section

Materials

Ammonia borane ($NH_3 \cdot BH_3$) was from Shanghai Macklin Biochemical Co., Ltd. Sodium acetate trihydrate ($CH_3COONa \cdot 3H_2O$) and Ammonium molybdate tetrahydrate ($(NH_4)_6Mo_7O_{24} \cdot 4H_2O$) were purchased from Shanghai Aladdin Chemistry Co., Ltd. Hydrogen peroxide (H_2O_2), nitric acid (HNO_3) and acetic acid (CH_3COOH) were purchased from Sinopharm Chemical Reagent Co., Ltd. 3,3′,5,5′-tetramethylbenzidine (TMB) and 1,2-diaminobenzene (OPD) were obtained from Energy Chemical Co., Ltd.

Catalyst characterizations

Transmission electron microscopy (TEM), high-angle annular dark-field scanning TEM (HAADF-STEM) and energy-dispersive X-ray spectroscopy (EDS) mapping images were acquired from a transmission electron microscope operated at 300 kV (Themis FEI). The SEM images were obtained by a scanning electron microscope (ZEISS Sigma 500, USA). The Pt content was determined by inductively coupled plasma optical emission spectrometer (ICP-OES). The X-ray absorption fine structure (XAFS) measurements were carried out at the BL14W1 station in Shanghai Synchrotron Radiation Facility. The X-ray diffraction (XRD) patterns were obtained by using Cu Kα radiation. X-ray photoelectron spectroscopy (XPS) measurements were conducted on an ESCALab-250 spectrometer with an Al Kα source (1486.6 eV). Diffuse reflectance infrared Fourier transform spectroscopy of CO chemisorption (CO-DRIFTS) and attenuated total reflection Fourier transform infrared (ATR-FTIR) spectra were recorded on a Bruker Vector 22 spectrometer. The determination of quantitative oxygen vacancy was performed on an electron Paramagnetic resonance (EPR) spectrometer under 77 K (Bruker A300-10/12), and the production of $\cdot OH$ and $\cdot O_2^-$ was determined on a Bruker EPR A300 spectrometer with 5,5-dimethyl-1-pyrroline N-oxide (DMPO) as the spin trap.

Catalyst synthesis

MoO_3 nanorods: Molybdenum trioxide was prepared by hydrothermal method.

Specifically, 15 mL of nitric acid (HNO_3) and 75 mL of water (H_2O) are fully mixed. Subsequently, 3.6 g ammonium molybdate tetrahydrate ($(NH_4)_6Mo_7O_{24}\cdot 4H_2O$) was added to the above mixed solvent, and then it was ultrasonically mixed for 30 min and transferred to a polytetrafluoroethylene-lined autoclave (250 mL), heated in an oven at 200 °C for 8 h. After the reaction, the product was centrifuged, thoroughly washed with water and ethanol, and vacuum dried at 60 °C overnight. Finally, the white product collected is MoO_3 nanorods.

Pt_n/MoO_3: Pt_n/MoO_3 was synthesized by ALD process in a self-made closed chamber ALD reactor. Specifically, the synthesized MoO_3 was uniformly coated on a quartz glass sheet and dried in air at room temperature. Pt ALD is carried out by sequentially exposing MoO_3 to $MeCpPtMe_3$ and ozone (O_3), where $MeCpPtMe_3$ acts as a platinum precursor and O_3 acts as an oxidant. The deposition temperature was set to 250 °C, and $MeCpPtMe_3$ was kept at 60 °C. Ultrapure nitrogen (99.999%) is used as carrier gas and purge gas. The loading of platinum was controlled by adjusting the number of Pt ALD cycles.

Pt_n/MoO_{3-x}-yR: Pt_n/MoO_{3-x}-yR was obtained by hydrogen activation. First, a certain amount of Pt_n/MoO_3 was placed in a porcelain boat, and then transferred to a tube furnace. The activated Pt_n/MoO_{3-x}-yR (y represents hydrotreatment temperature) catalysts were obtained by hydrogen treatment (10% H_2/Ar, 2 h) at 50, 150, 250 and 350 °C, respectively.

Catalyst evaluation

Hydrolytic dehydrogenation of AB: A certain amount of catalysts and deionized water (usually 10 mL) were added to a round-bottom flask, and then AB was added under magnetic stirring to react at 25 °C. A U-shaped burette filled with water is used to systematically measure the volume of hydrogen generated by monitoring the change of water level. For the stability experiment, the same amount of AB is added to the reactor after the residual H_2 in the reaction system is exhausted. For the isotope effect experiment, the deionized water in the above reaction was replaced with an equal amount of D_2O, and other reaction conditions remained unchanged.

Catalytic oxidation of H_2O_2: The production of free radicals from H_2O_2 catalyzed by the catalyst was determined by two color reactions (TMB and OPD). TMB color reaction: In a typical experiment, a certain amount of catalyst was added to the buffer solution of HAc-NaAc (0.1M, pH = 5.0) and mixed uniformly by ultrasound. Then H_2O_2 was added to make the final concentration of 1 mM (2 mL reaction system). Finally, TMB was added to the final concentration of 10 mM under stirring conditions. Finally, the resulting mixture was incubated at 37 °C and the absorbance at 652 nm was measured over time. For the determination of the kinetic curve of H_2O_2, the absorbance at 652 nm was compared by changing the concentration of H_2O_2 and keeping other conditions unchanged. The performance of the catalyst in catalyzing the H_2O_2 reaction was also evaluated using OPD as a substrate. The experimental process is similar to H_2O_2-TMB system except that the curve of the ultraviolet peak of ox-OPD at 450 nm with time was monitored by ultraviolet spectrophotometer.

Determination of free radicals: To test the free radicals generated by the catalyst catalyzing hydrogen peroxide, MB (5 μg/mL), H_2O_2 (40 mM) and Pt_n/MoO_{3-x}-150R (200 μg/mL) were dispersed in a pH = 5.0 HAc-NaAc buffer solution (2 mL). Nanodrop was used to record the absorbance at 665 nm at different time points. In addition, the DMPO capture agent was used to detect the free radicals produced by the catalyst catalyzing hydrogen peroxide, and the free radical signal in the reaction process was detected by EPR.

Methods

The DFT calculations were carried out using the Vienna Ab initio Simulation Package (VASP).[1,2] The electron–ion interactions were described using the projector-augmented wave (PAW).[3,4] The Perdew–Burke–Ernzerhof (PBE) functional within the generalized gradient approximation (GGA) was used to describe the potentials and the electron exchange–correlation energy.[5,6] The D3 dispersion correction was applied to describe the van der Waals interactions. The plane wave cutoff energy was set to 400 eV, and electron smearing via a 2nd-order Methfessel-Paxton[7] technique with the width of 0.2 eV was employed to ensure the energy errors less than 1 meV/atom. The adsorption energy (E_{ads}) of the surface species is calculated by $E_{ads} = E_{species + surface} - E_{species} - E_{surface}$, where $E_{species+surface}$ is the total energy of the adsorbed species with catalyst, $E_{surface}$ and $E_{species}$ represent the energy of the unoccupied surface and species in the gas phase, respectively.

Models

The MoO_3 unit cell was modeled as an orthorhombic structure with Pbnm symmetry, supported by TEM and XRD results. The $MoO_3(010)$ facet was built to simulate the material surface because it has the lowest surface energy and exposes the Mo=O terminal and Mo-O-Mo bridge oxygen sites[8]. The p (3 × 3) supercells which contain 54 O atoms and 18 Mo atoms were used for the surface model. The top two layers along with adsorbates were allowed to relax and the bottom two layers were fixed in their bulk positions. To avoid significant slab interaction the vacuum gap space between slabs was set to 15 Å, excluding the adsorbates. According to the lattice sizes, 2 × 2 × 1 k-point grid sampling within the Brillouin zones was set.

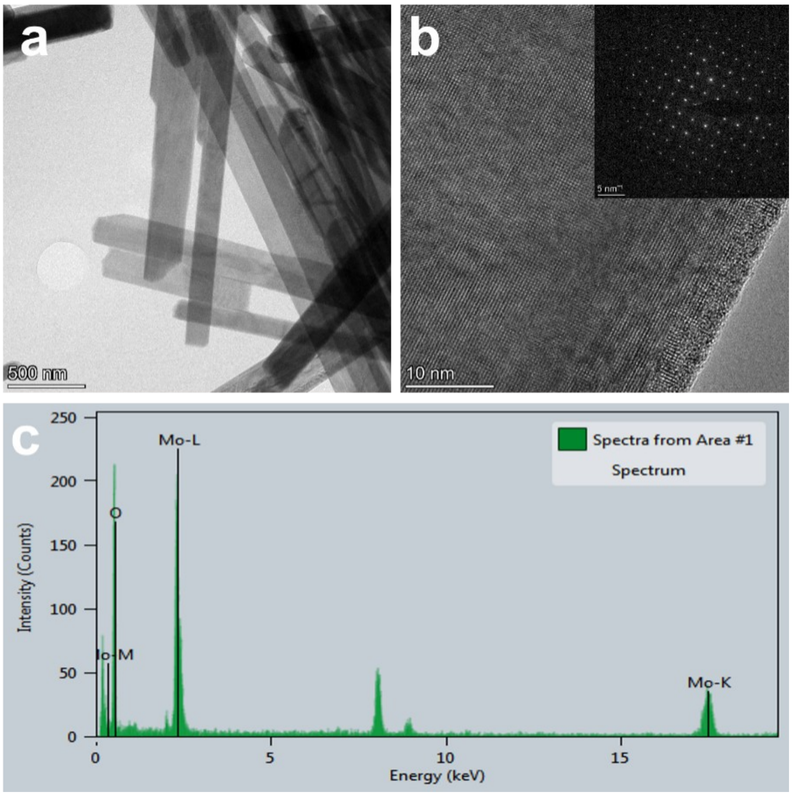

Fig. S1. (a) TEM, (b) HRTEM images (Inset is selected area electron diffraction pattern) and (c) EDS energy spectrum of MoO_3 nanorods. The length and width of MoO_3 nanorods are approximately 7 μm and 200 nm, respectively.

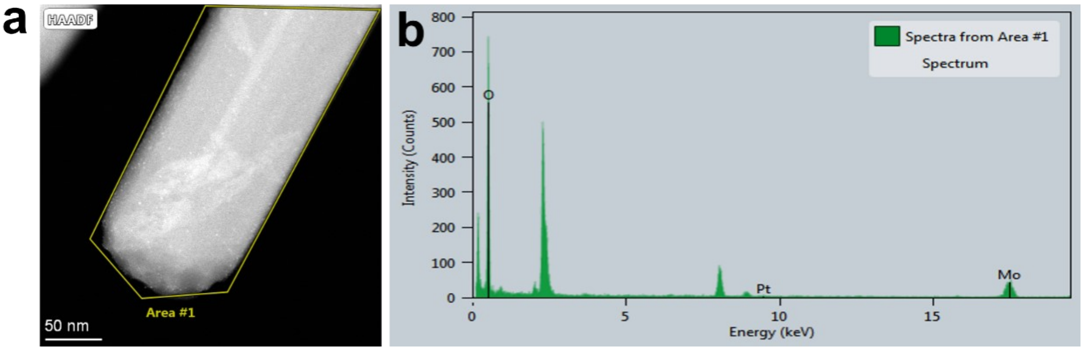

Fig. S2. (a) HAADF-STEM image and (b) EDS energy spectrum of Pt_n/MoO_3 catalysts.

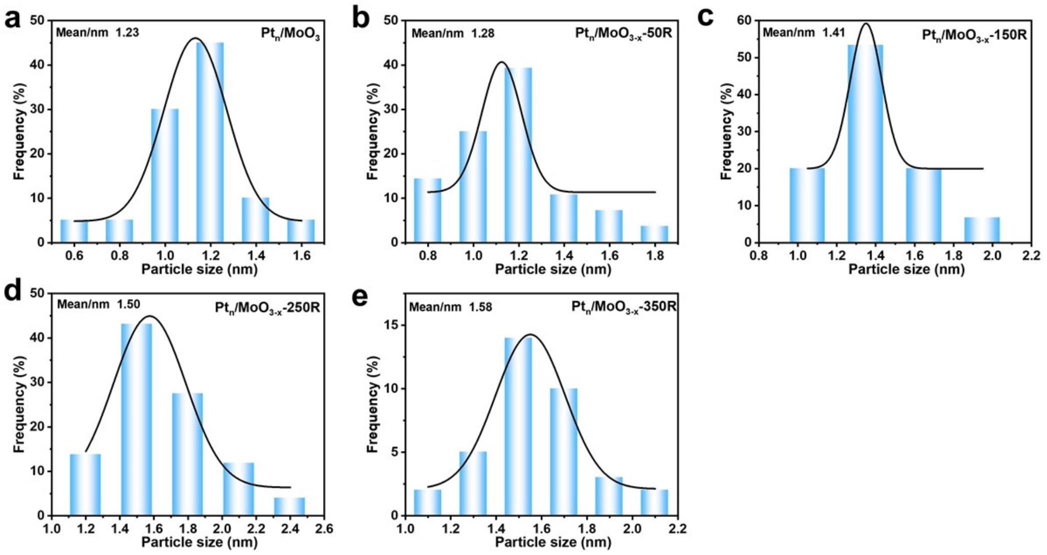

Fig. S3 (a-e) The particle size distribution statistics of the catalysts.

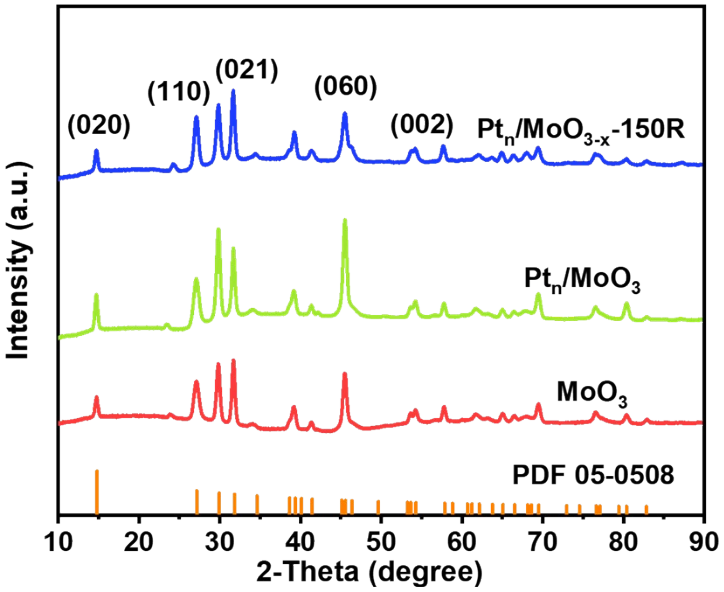

Fig. S4. XRD patterns of MoO$_3$, Pt$_n$/MoO$_3$ and Pt$_n$/MoO$_{3-x}$-150R catalysts.

The peaks observed at 14.8°, 27.2°, 31.9°, 45.6°, and 57.9° can be assigned to the (020), (110), (021), (060) and (002) crystallographic planes of orthorhombic MoO$_3$, respectively. Notably, no diffraction peaks corresponding to Pt species were detected due to the low loading and the high dispersion of Pt clusters.

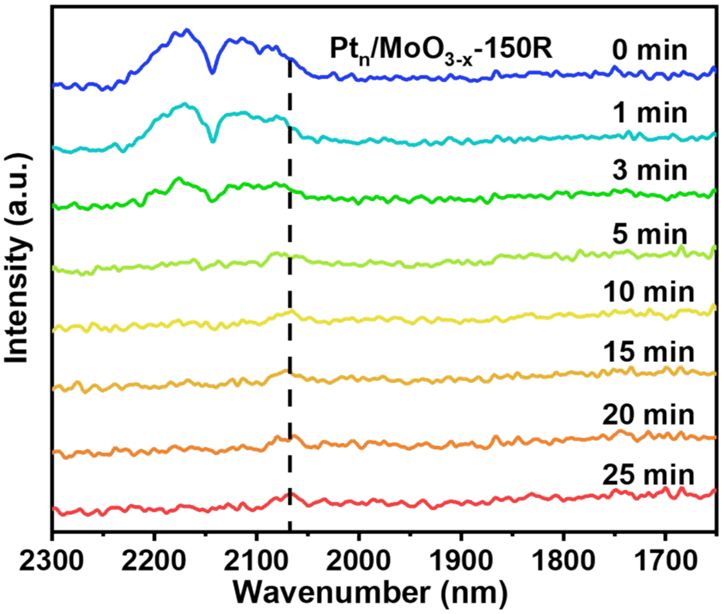

Fig. S5. In situ CO-DRIFT spectra of Pt$_n$/MoO$_{3\text{-}x}$-150R catalysts.

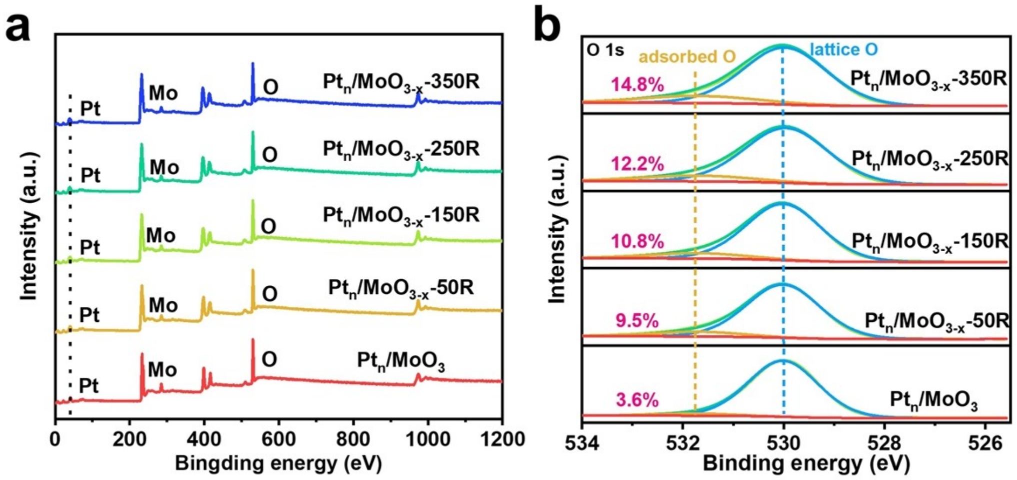

Fig. S6. (a) Full spectra and (b) O1s XPS spectra of Pt_n/MoO_3 and Pt_n/MoO_{3-x}-yR catalysts.

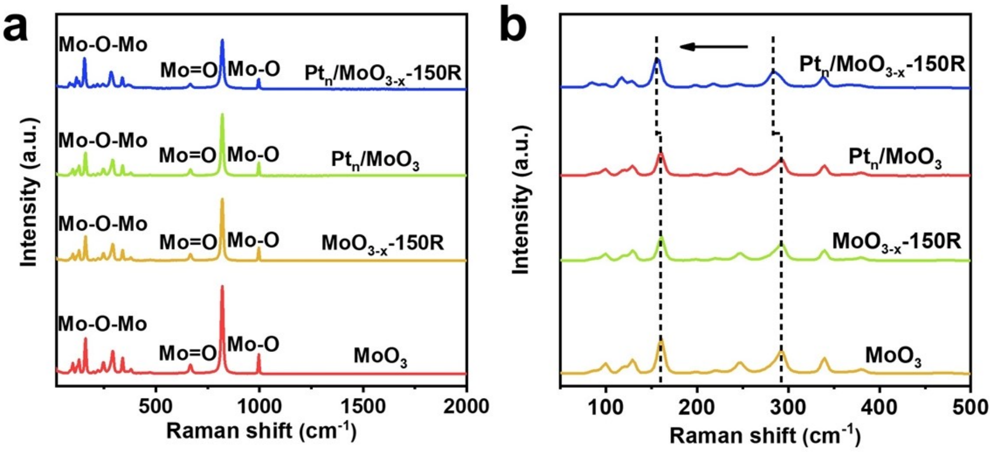

Fig. S7. (a) Raman spectra and (b) corresponding amplified spectra of the MoO$_3$, MoO$_{3-x}$-150R, Pt$_n$/MoO$_3$ and Pt$_n$/MoO$_{3-x}$-150R catalysts.

The Raman peaks at 994 and 818 cm^{-1} are attributed to the stretching vibrations of Mo-O bonds in MoO$_3$. The peak at 160 cm^{-1} corresponds to the bending mode of Mo-O-Mo, while the peak at 665 cm^{-1} originates from the stretching vibration of terminal Mo=O bond.

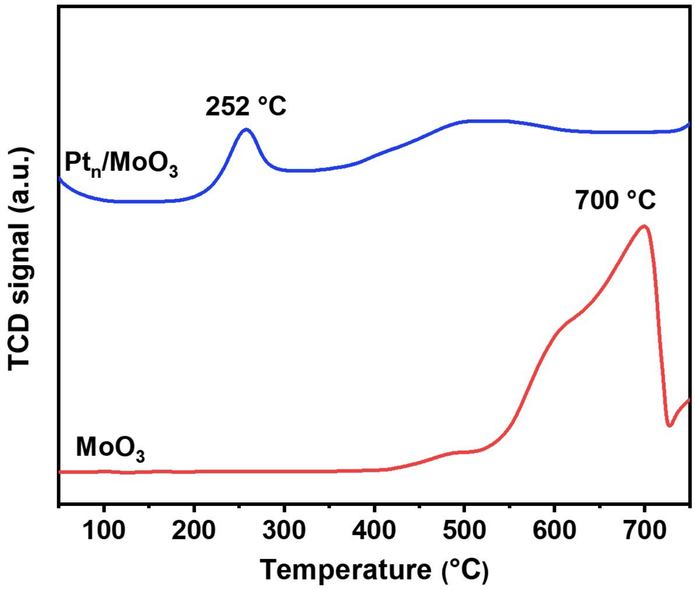

Fig. S8. H_2-TPR profiles of the MoO_3 and Pt_n/MoO_3 catalysts.

The reduction of bare MoO_3 needs a much higher temperature (around 700 °C). Remarkably, the reduction temperature of Pt_n/MoO_3 significantly decreases to 252 °C, demonstrating that Pt clusters can facilitate hydrogen dissociation and subsequent spillover to MoO_3. This observed redshift further indicates a structural transformation of MoO_3 from long-range ordered to short-range disordered configuration, which is typically accompanied by the formation of oxygen vacancies (Ov).

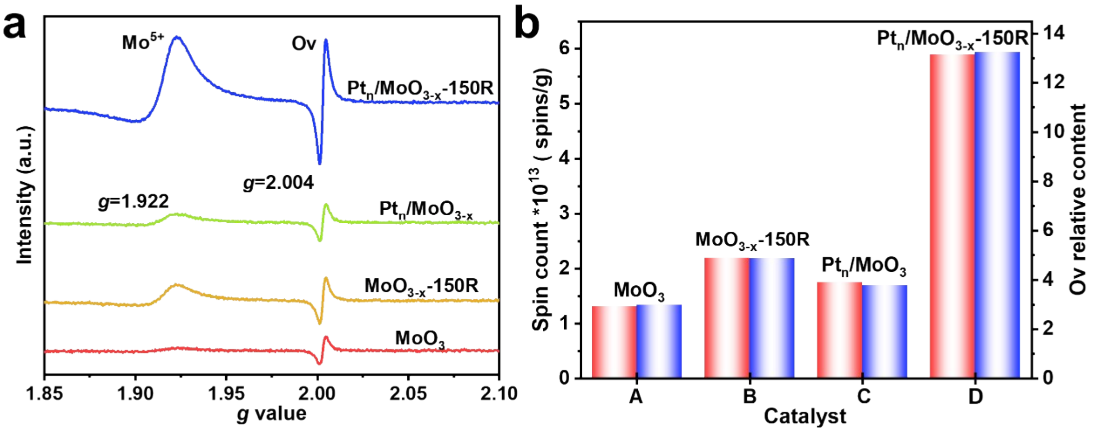

Fig. S9. (a) EPR spectra of MoO$_3$, MoO$_{3-x}$-150R, Pt$_n$/MoO$_3$ and Pt$_n$/MoO$_{3-x}$-150R catalysts. (b) Ov concentration and electron spin number of MoO$_3$, MoO$_{3-x}$-150R, Pt$_n$/MoO$_3$ and Pt$_n$/MoO$_{3-x}$-150R catalysts (with 1,1-Diphenyl-2-picrylhydrazyl as standard substance).

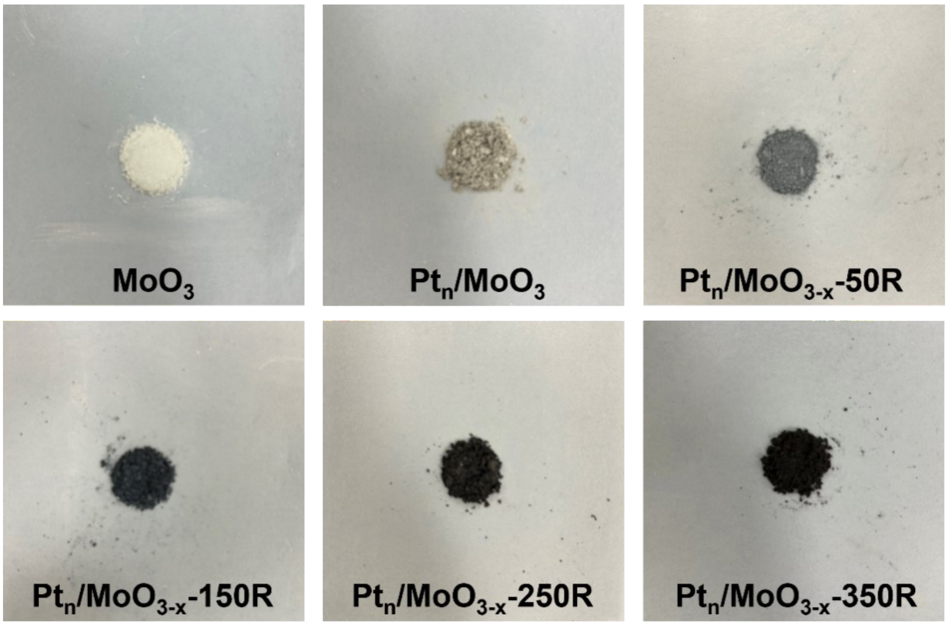

Fig. S10. Color changes of MoO$_3$, Pt$_n$/MoO$_3$ and Pt$_n$/MoO$_{3-x}$-yR catalysts.

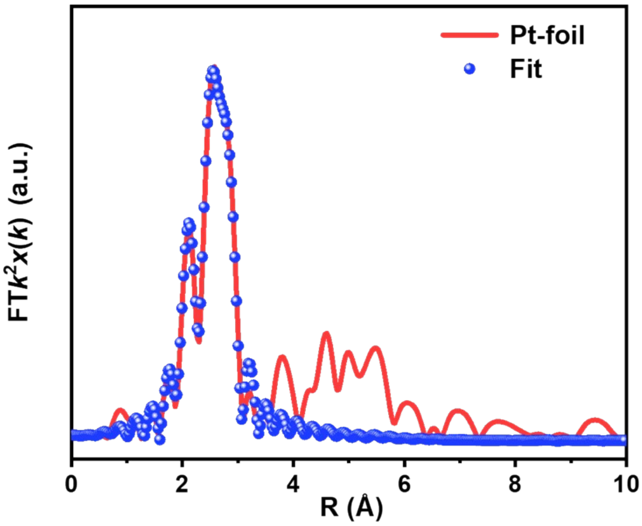

Fig. S11. EXAFS R-space fitting curves (blue ball) for the Pt foil.

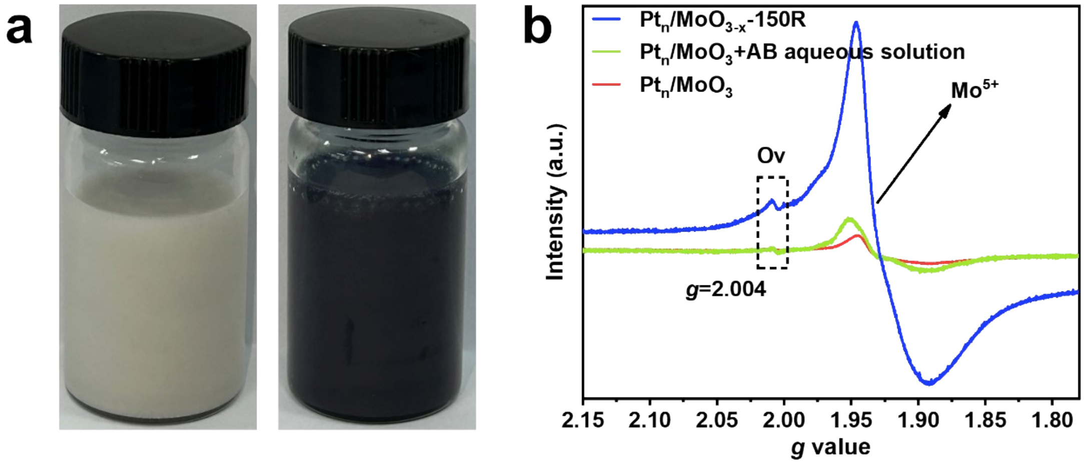

Fig. S12. (a) Color change during in-situ reaction. (b) EPR spectra of Pt_n/MoO_3 catalyst under reducing conditions and in situ catalytic conditions for hydrogen production from AB.

The obvious color transition was observed during the reaction due to the generation of Ov by in situ generated active hydrogen species (Fig. S12a). However, their contribution is much weaker than the hydrogen spillover effect during the gaseous hydrotreatment process, which can lead to the generation of more Ov (Fig. S12b). Therefore, the synergy between Pt cluster and Ov contributes to the boosted H_2 evolution activity.

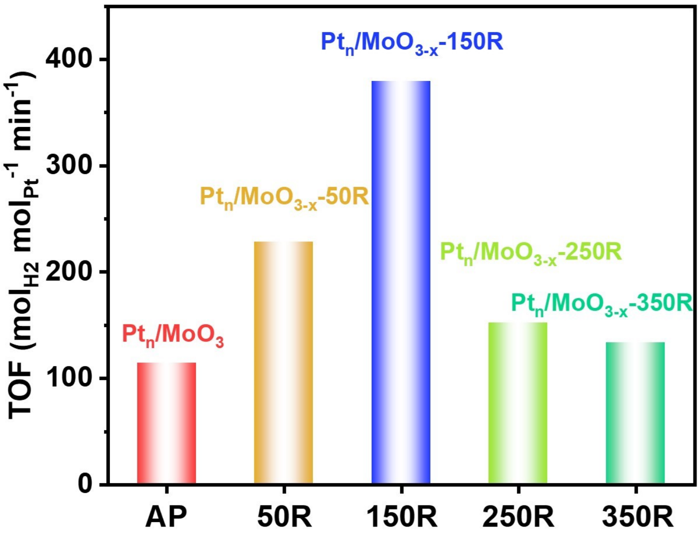

Fig. S13. TOF values of Pt_n/MoO_3 and Pt_n/MoO_{3-x}-yR catalysts in hydrolytic dehydrogenation of AB.

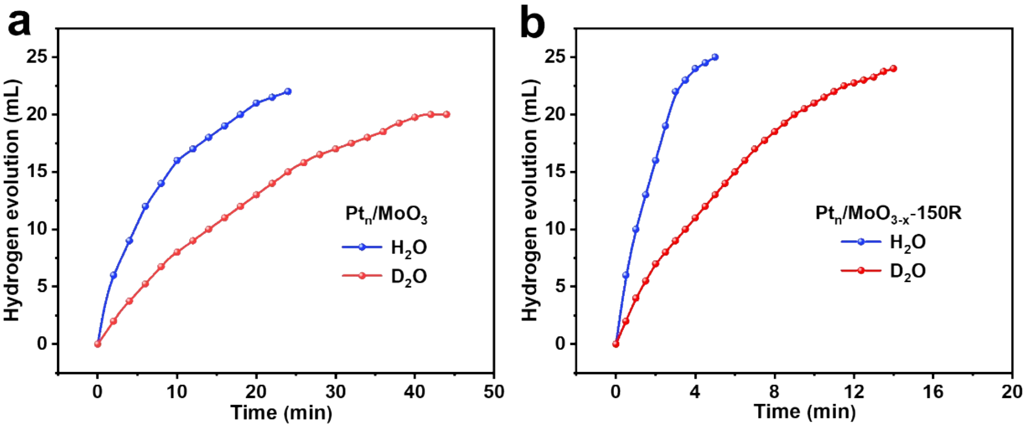

Fig. S14. The measurements of KIE values over the (a) Pt$_n$/MoO$_3$ and (b) Pt$_n$/MoO$_{3-x}$-150R catalysts.

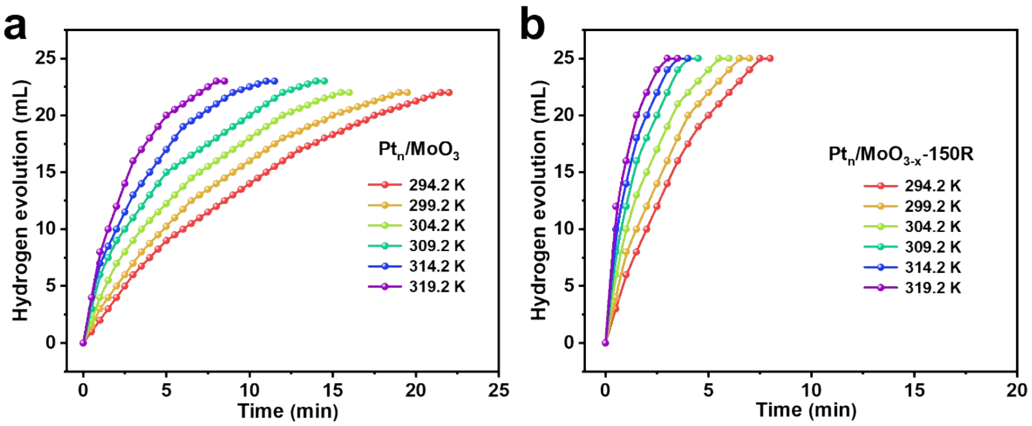

Fig. S15. Volume of hydrogen evolved as a function of time under different temperatures catalyzed by the (a) Pt$_n$/MoO$_3$ and (b) Pt$_n$/MoO$_{3-x}$-150R catalysts.

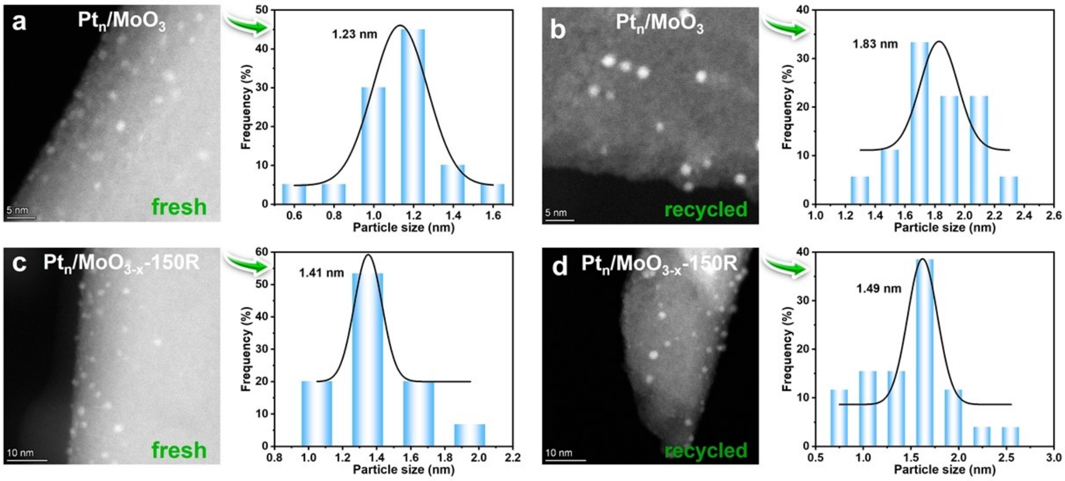

Fig. S16. The Morphology changes and corresponding particle size distribution statistics of the Pt_n/MoO_3 catalyst (a) before and (b) after five catalytic cycles. The Morphology changes and corresponding particle size distribution statistics of the Pt_n/MoO_{3-x}-150R catalyst (c) before and (d) after five catalytic cycles.

From the HAADF-STEM images of the fresh and recycled Pt_n/MoO_3 (Figs. S16a and 16b), severe detachment and size aggregation of Pt species can be observed. However, for the Pt_n/MoO_{3-x}-150R catalyst (Figs. 16c and 16d), these phenomena are significantly inhibited due to the anchoring effect of Ov toward Pt clusters, consisting well with the above results of excellent cycling stability and much-inhibited Pt leaching over Pt_n/MoO_{3-x}-150R catalysts.

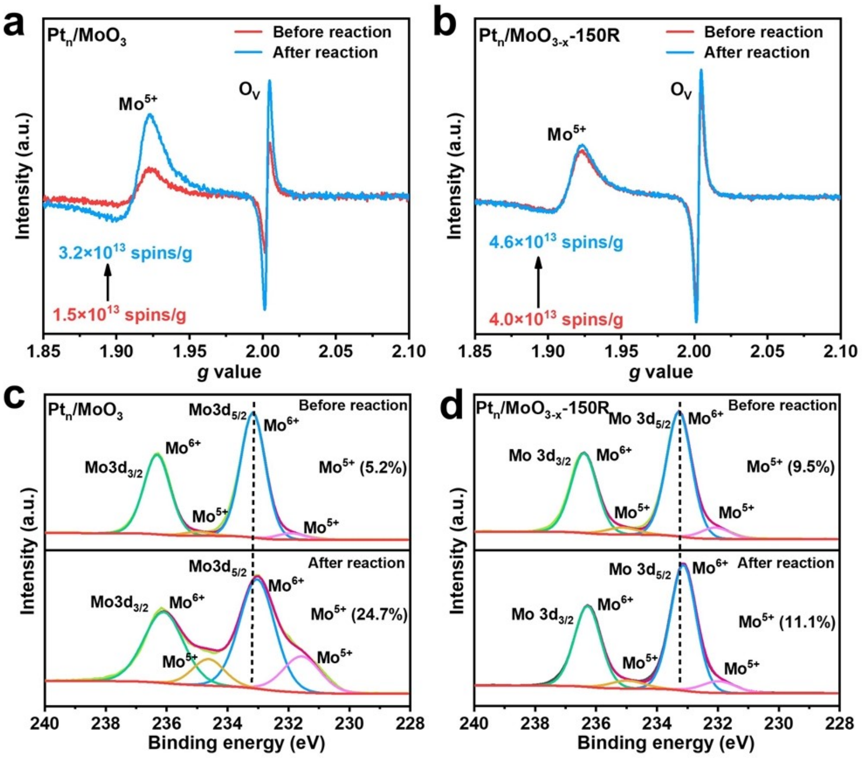

Fig. S17. The EPR spectra of (a) Pt_n/MoO_3 and (b) Pt_n/MoO_{3-x}-150R catalysts before and after five catalytic cycles. The Mo 3d XPS spectra of (c) Pt_n/MoO_3 and (d) Pt_n/MoO_{3-x}-150R catalysts before and after five catalytic cycles.

EPR analysis before and after the five catalytic cycles revealed that a certain amount of O_V is newly formed for the Pt_n/MoO_3 catalyst (Fig. S17a). However, the O_V concentration in the activated Pt_n/MoO_{3-x}-150R catalysts are almost unchanged before and after five catalytic cycles (Fig. S17b). Besides, the XPS analysis further corroborated these findings: the proportion of Mo^{5+} in the Pt_n/MoO_3 catalyst increased notably after five catalytic cycles (Fig. S17c), whereas the proportion changes of Mo^{5+} in the Pt_n/MoO_{3-x}-150R catalyst are almost negligible (Fig. S17d). Therefore, activation treatment toward Pt_n/MoO_3 is an indispensable step to modulate Ov concentration and boost catalytic activity and stability.

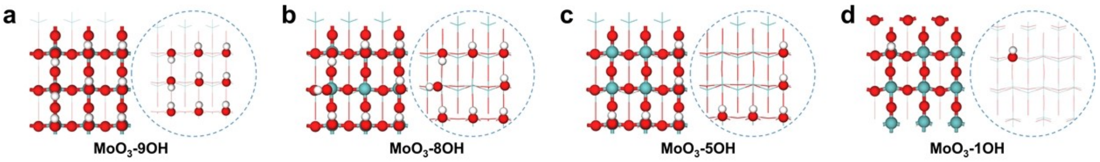

Fig. S18. The surface structures of (a) MoO_3-9OH, (b) MoO_3-8OH, (c) MoO_3-5OH and (d) MoO_3-1OH. Color code: H (white), O (red), Mo (cyan).

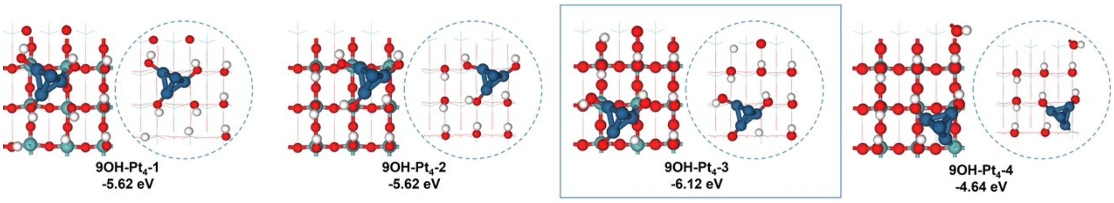

Fig. S19. The structures and adsorption energies of Pt_4 cluster decorated on the MoO_3-9OH. The optimal configuration is highlighted with the rectangle. Color code: H (white), O (red), Mo (cyan), Pt (dark blue).

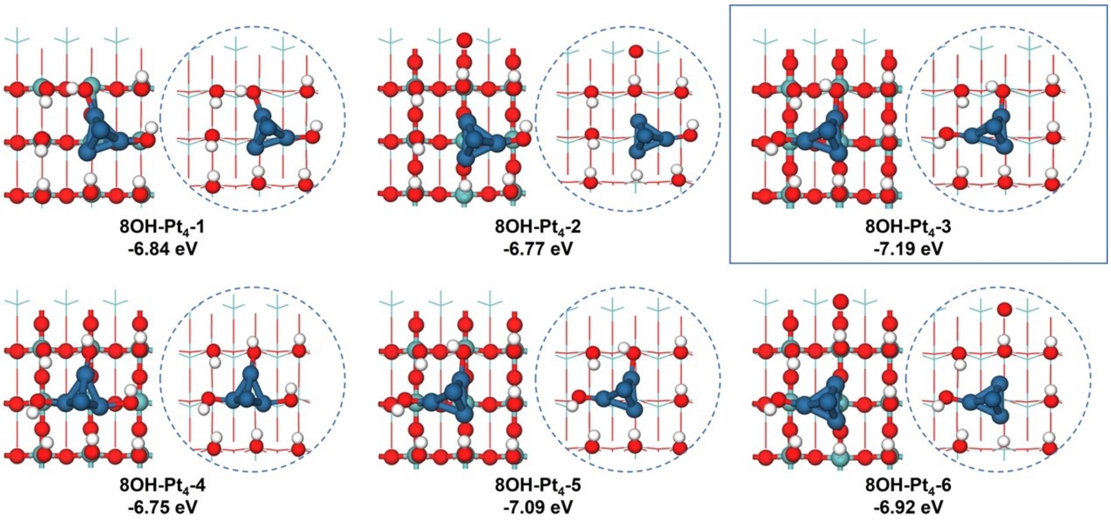

8OH-Pt_4-1 -6.84 eV

8OH-Pt_4-2 -6.77 eV

8OH-Pt_4-3 -7.19 eV

8OH-Pt_4-4 -6.75 eV

8OH-Pt_4-5 -7.09 eV

8OH-Pt_4-6 -6.92 eV

Fig. S20. The structures and adsorption energies of Pt_4 cluster decorated on the MoO_3-8OH. The optimal configuration is highlighted with the rectangle.

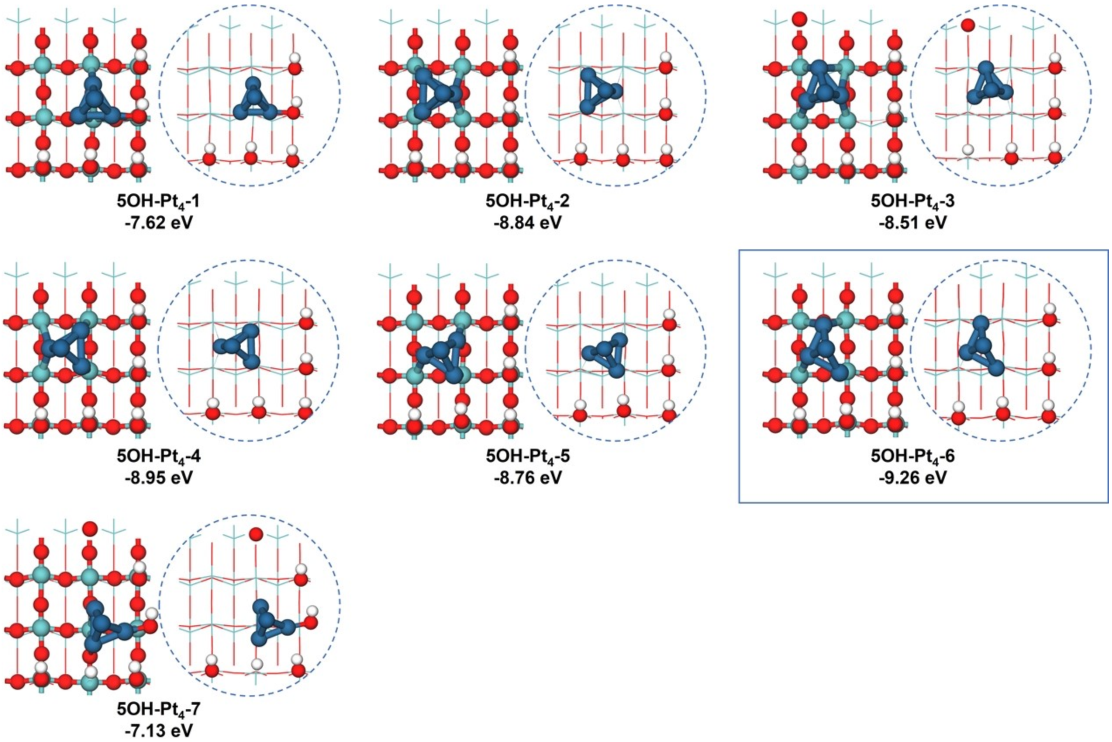

Fig. S21. The structures and adsorption energies of Pt_4 cluster decorated on the MoO_3-5OH.

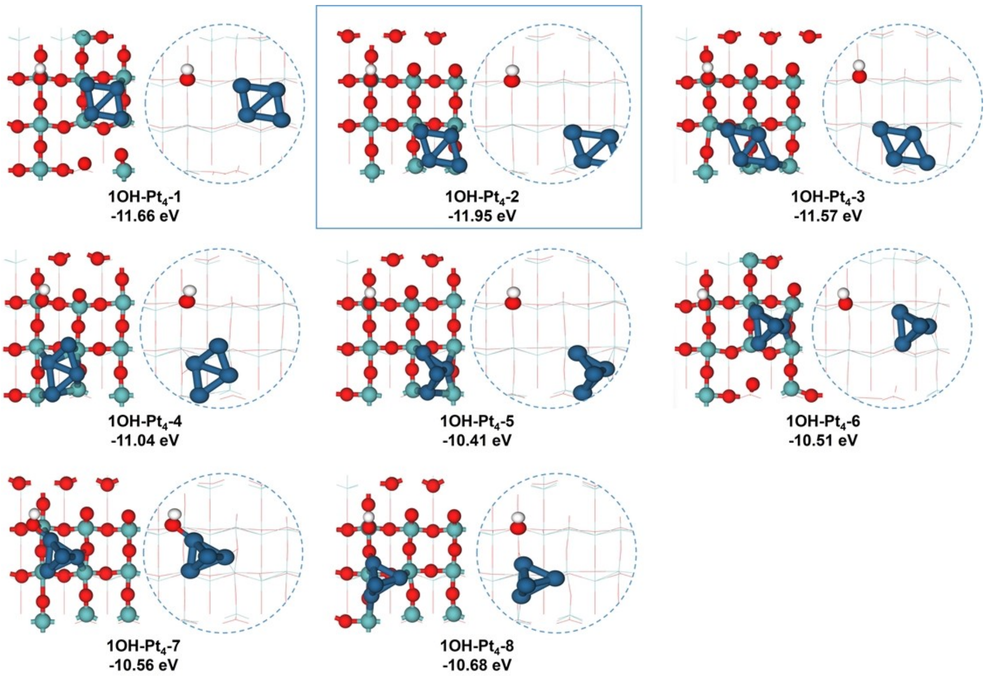

Fig. S22. The structures and adsorption energies of Pt_4 cluster decorated on the MoO_3-1OH.

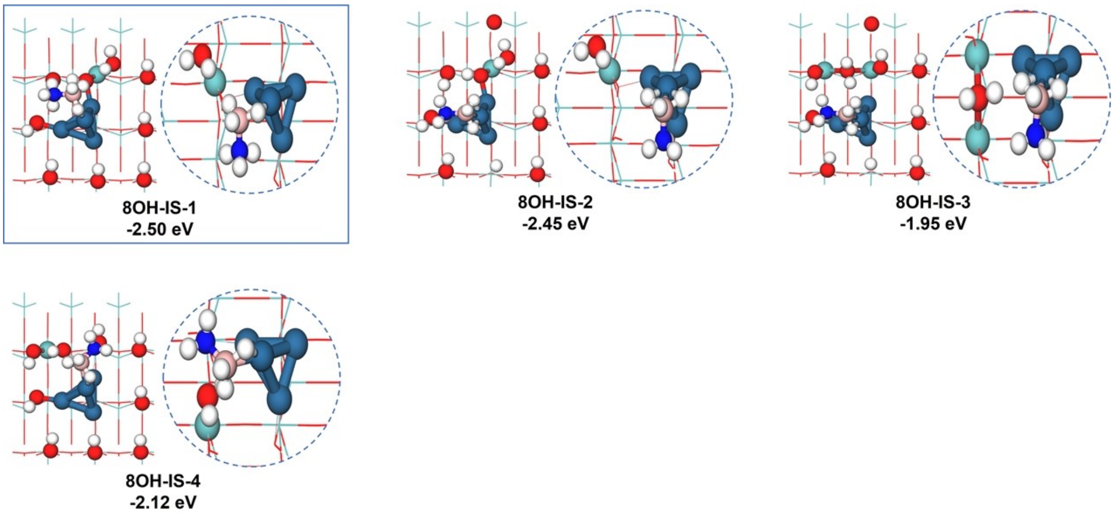

8OH-IS-1
-2.50 eV

8OH-IS-2
-2.45 eV

8OH-IS-3
-1.95 eV

8OH-IS-4
-2.12 eV

Fig. S23. The structures and adsorption energies of the initial states (co-adsorption) on the Pt_n/MoO_3-8OH surface. The H, O, Mo, Pt, N, B atoms are denoted white, red, cyan, dark blue, blue and pink balls, respectively.

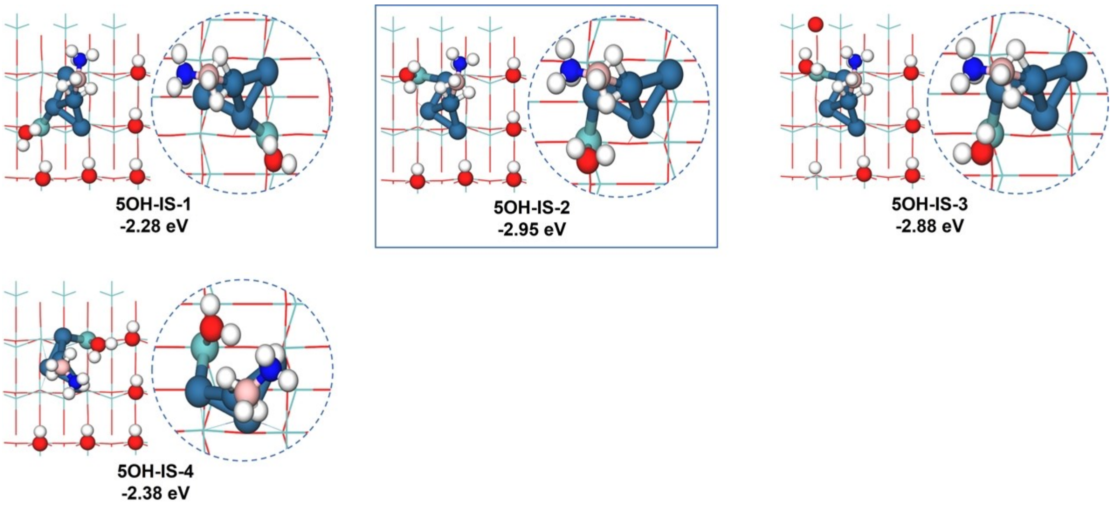

Fig. S24. The structures and adsorption energies of the initial states (co-adsorption) on the Pt_n/MoO_3-5OH surface.

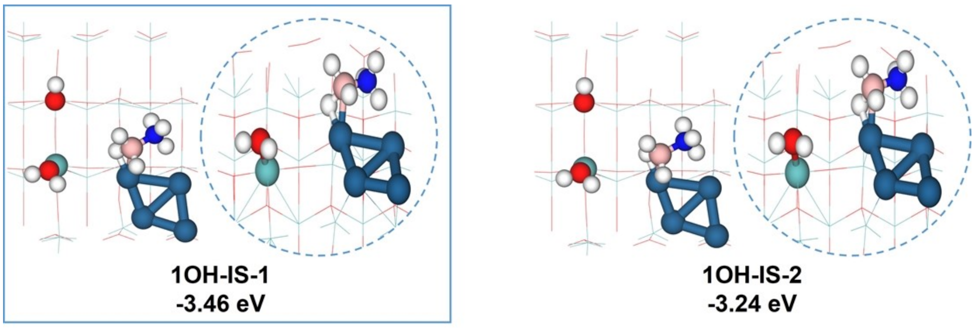

1OH-IS-1
-3.46 eV

1OH-IS-2
-3.24 eV

Fig. S25. The structures and adsorption energies of the initial states (co-adsorption) on the Pt_n/MoO_3-1OH surface.

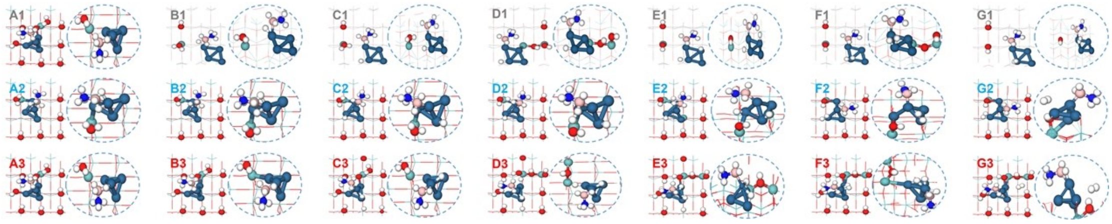

Fig. S26. The structures for NH_3BH_3 and H_2O dehydrogenation on the Pt_n/MoO_3-1OH Pt_n/MoO_3-5OH and Pt_n/MoO_3-8OH catalyst models.

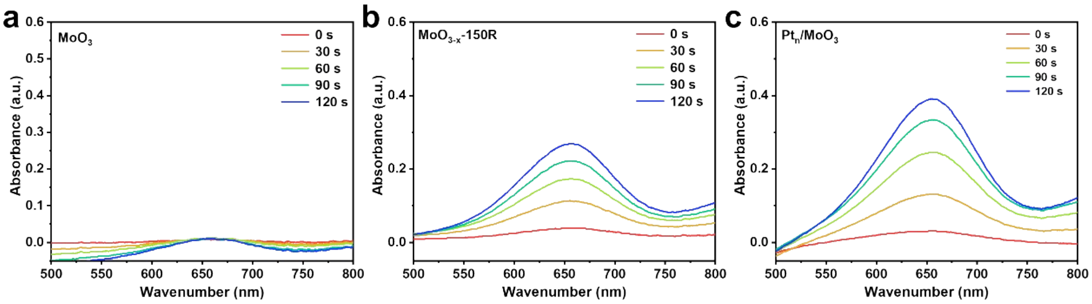

Fig. S27. The UV-vis absorption spectra of H_2O_2-TMB system catalyzed by (a) MoO_3, (b) MoO_{3-x}-150R and (c) Pt_n/MoO_3 catalysts.

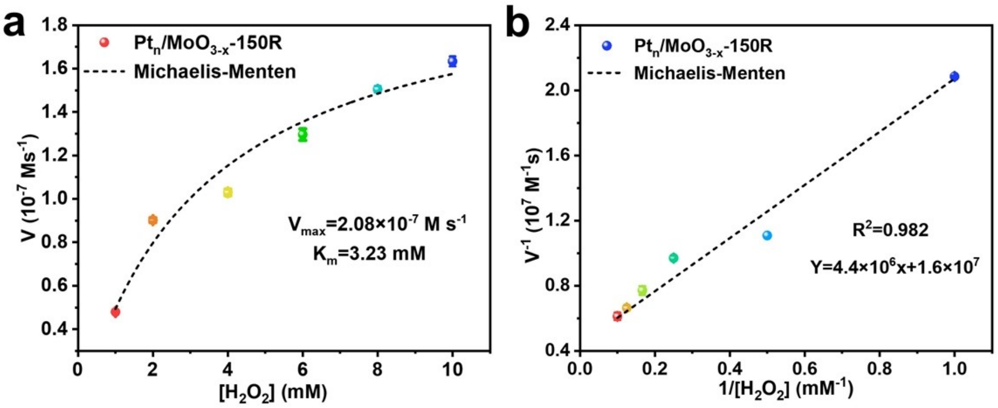

Fig. S28. (a) The Michaeli-Menten kinetics at various H_2O_2 concentrations catalyzed by Pt_n/MoO_{3-x}-150R catalysts. (b) The Lineweaver Burk plot of 1/V vs 1/[H_2O_2] over the Pt_n/MoO_{3-x}-150R catalysts.

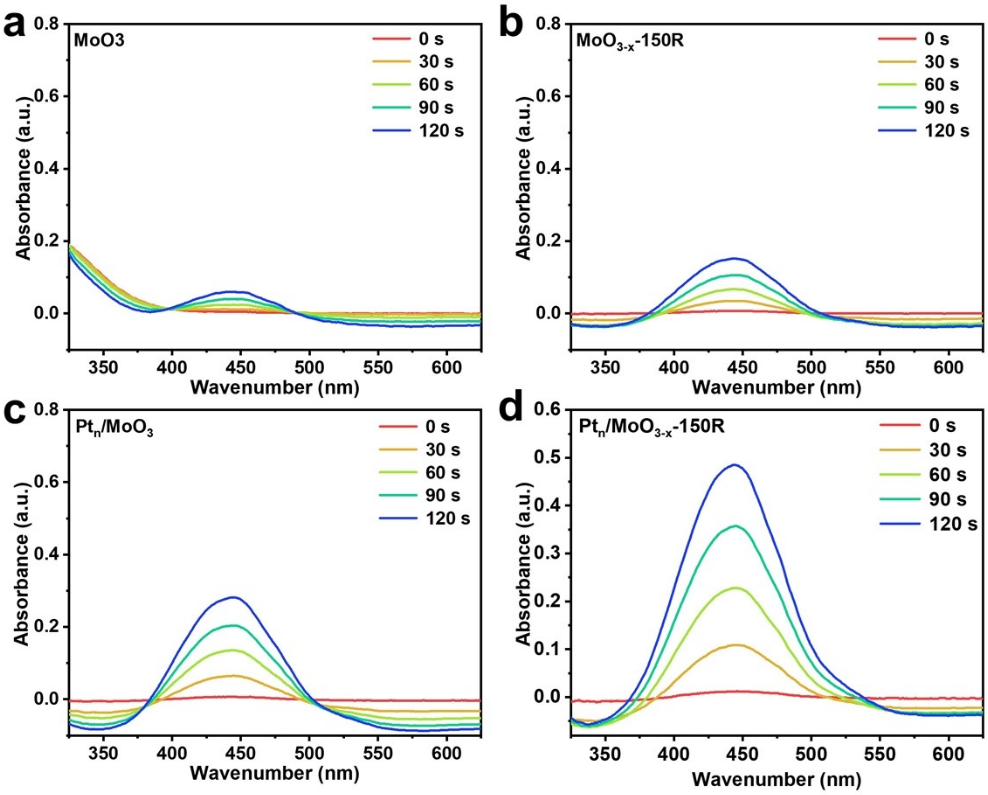

Fig. S29. The UV-vis absorption spectra of H_2O_2-OPD catalyzed by (a) MoO_3, (b) MoO_{3-x}-150R, (c) Pt_n/MoO_3 and (d) Pt_n/MoO_{3-x}-150R catalysts.

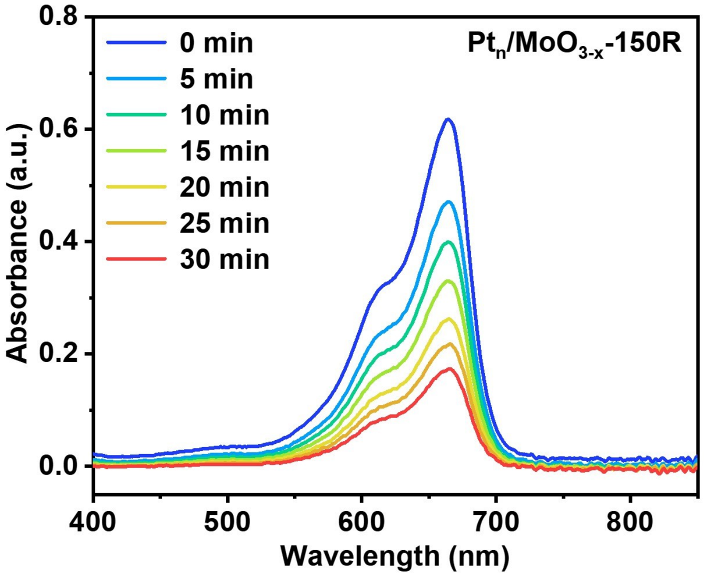

Fig. S30. Time dependent MB degradation activity catalyzed by Pt$_n$/MoO$_{3-x}$-150R catalysts.

Table S1. Pt loadings of different catalysts determined by ICP-OES.

Catalysts	**Pt loadings (wt%)**
Pt_n/MoO_3	0.42
Pt_n/MoO_{3-x}-50R	0.45
Pt_n/MoO_{3-x}-150R	0.44
Pt_n/MoO_{3-x}-250R	0.43
Pt_n/MoO_{3-x}-350R	0.44

Table S2. Activity comparison of the Pt-based catalysts tested in the hydrolytic reaction of AB ever reported.

Catalysts	Temperatures	n_{Pt}/n_{AB}	TOF[a]	References
Pt/γ-Al_2O_3	25 °C	0.018	222	8
Pt/CeO_2	25 °C	0.018	182	9
Pt@MIL-101	25 °C	0.0029	414	10
Pt/CNTs-O-HT	25 °C	0.0047	468	11
Pt25@TiO_2	25 °C	0.0016	311	12
Ptn/MoO_{3-x}-150R	25 °C	0.0028	379	This work
$Ni_{0.33}$@$Pt_{0.67}$/C	25 °C	0.018	81	13
Pt@Co/mCN	35 °C	0.004	118	14
NiPt(1:3)	RT[b]	0.05	84.1	15
Pt_1/Co_3O_4	25 °C	0.0008	1220	16
KB-CuPt	25 °C	0.002	859	17
Ni_2Pt@ZIF-8	RT	0.01	2222.2[c]	18
$Pt_{0.5}Ru_{0.5}$/CNT	25 °C	--	546	19
PtCo/SAPO-34	30 °C	0.0079	262	20

[a] The TOF unit is $mol_{H2}\ mol_{Pt}^{-1}\ min^{-1}$.

[b] RT represents room temperature.

[c] The value is obtained under the addition of 0.3 M of NaOH.

References

1 G. Kresse, J. Furthmüller, J. *Comput. Mater. Sci.*, 1996, **6**, 15-50.

2 G. Kresse, J. Furthmüller, *Phys. Rev. B*, 1996, **54**, 11169-11186.

3 P. E. Blochl, *Phys. Rev. B*, 1994, **50**, 17953-17979.

4 G. Kresse, *Phys. Rev. B*, 1999, **59**, 1758-1775.

5 J. P. Perdew, K. M. Burke, Ernzerhof, *Phys. Rev. Lett.*, 1996, **77**, 3865-3868.

6 J. P. Perdew, Y. Wang, *Phys. Rev. B*, 1992, **45**, 13244-13249.

7 M. Methfessel, A. T. Paxton, *Phys. Rev. B*, 1989, **40**, 3616-3621.

8 M. Chandra, Q. Xu, *J. Power Sources*, 2007, **168**, 135-142.

9 X. Wang, D. Liu, S. Song, H. Zhang, *Chem. Commun.*, 2012, **48**, 10207-10209.

10 A. Aijaz, A. Karkamkar, Y. J. Choi, N. Tsumori, E. Rönnebro, T. Autrey, H. Shioyama, Q. Xu, *J. Am. Chem. Soc.*, 2012, **134**, 13926-13929.

11 W. Chen, J. Ji, X. Duan, G. Qian, P. Li, X. Zhou, D. Chen, W. Yuan, *Chem. Commun.*, 2014, **50**, 2142-2144.

12 M. Khalily, H. Eren, S. Akbayrak, H. Susapto, N. Biyikli, S. Özkar, M. Guler, *Angew. Chem. Int. Ed.*, 2016, **128**, 12445-12449.

13 X. Yang, F. Cheng, J. Liang, Z. Tao, J. Chen, *Int. J. Hydrogen Energy*, 2011, **36**, 1984-1990.

14 X. Cui, H. Li, G. Yu, M. Yuan, J. Yang, D. Xu, Y. Hou, Z. Dong, *Int. J. Hydrogen Energy*, 2017, **42**, 27055-27065.

15 O. Ramírez, S. Bonardd, C. Saldías, M. Kroff, J. O'Shea, D. Díaz, A. Leiva, *Int. J. Hydrogen Energy*, 2023, **225**, 494-502.

16 J. Li, Q. Guan, H. Wu, W. Liu, Y. Lin, Z. Sun, X. Ye, X. Zheng, H. Pan, J. Zhu, S. Chen, W. Zhang, S. Wei, J. Lu, *J. Am. Chem. Soc.*, 2019, **141**, 14515.

17 T. Karaca, M. Sevim, Ö. Metin, *ChemCatChem* 2017, **9**, 4185-4190.

18 F. Fu, C. Wang, Q. Wang, A. Martinez-Villacorta, A. Escobar, H. Chong, X. Wang, S. Moya, L. Salmon, E. Fouquet, J. Ruiz, D. Astruc, *J. Am. Chem. Soc.*, 2018, **140**, 10034-10042.

19 W. Chen, D. Li, C. Peng, G. Qian, X. Duan, D. Chen, X. Zhou, *J. Catal.*, 2017, **356**, 186-196.

20 W. Cong, H. Zhang, L. Bing, F. Wang, D. Han, G. Wang, *J. Alloy. Compd.*, 2023, **956**, 170314.